A&A manuscript no.
(will be inserted by hand later)

Your thesaurus codes are:
02(11.03.4 MG2016+112; 11.03.4 AXJ2019+112; 12.04.1; 12.07.1)

ASTRONOMY AND ASTROPHYSICS
January 17, 2000

Weak lensing observations of the "dark" cluster MG2016+112

D. Clowe[1], **N. Trentham**[2], **and J. Tonry**[⋆3]

[1] Max-Planck-Institut fuer Astrophysik, Karl Schwarzschild Str. 1, 85740 Garching, Germany
[2] Institute of Astronomy, University of Cambridge, Madingley Road, Cambridge. CB3 0HA, United Kingdom
[3] Institute for Astronomy, University of Hawaii, 2680 Woodlawn Drive, Honolulu, HI 96822, USA

Received 10 January 2000 / Accepted 10 January 2000

Abstract. We investigate the possible existence of a high-redshift ($z = 1$) cluster of galaxies associated with the QSO lens system MG2016+112. From an ultra-deep R- and less deep V- and I-band Keck images and a K-band mosaic from UKIRT, we detect ten galaxies with colors consistent with the lensing galaxy within $225h^{-1}$ kpc of the $z = 1.01$ lensing galaxy. This represents an overdensity of more than ten times the number density of galaxies with similar colors in the rest of the image. We also find a group of seven much fainter objects closely packed in a group only $27h^{-1}$ kpc north-west of the lensing galaxy. We perform a weak lensing analysis on faint galaxies in the R-band image and detect a mass peak of a size similar to the mass inferred from X-ray observations of the field, but located $64''$ northwest of the lensing galaxy. From the weak lensing data we rule out a similar sized mass peak centered on the lensing galaxy at the 2σ level.

Key words: Galaxies: clusters: individual: MG2016+112 – Galaxies: clusters: individual: AXJ2019+112 – dark matter – gravitational lensing

1. Introduction

The QSO lens MG2016+112 is a long-standing enigma. Spanning a few arcseconds in size, the system contains two QSO images (designated as components A and B, see Fig. 4) and an extended structure (designated C), all at redshift $z = 3.273$ (Lawrence et al. 1984, Schneider et al. 1985, 1986). The extended structure appears as an arc in the infrared (Langston et al. 1991; Lawrence et al. 1993; Benitez et al. 2000, hereafter B99), but consists of four subcomponents in the radio, elongated along the arc (Garrett et al. 1996). Roughly in the middle of the lens structure is a giant elliptical galaxy at redshift $z = 1.01$ (designated D, Schneider et al. 1985), and another galaxy of unknown redshift lies just outside the giant arc. Various lensing models have been applied to this system involving a single elliptical galaxy as lens, a giant elliptical galaxy plus a cluster core lens, a giant elliptical plus companion galaxy lens, and a double lens model involving two galaxies at different redshift each lensing parts of the system (Narasimha & Chitre 1989; Langston et al. 1991; Nair & Garrett 1997; B99), but no model has successfully reproduced all of the observed structures, positions, and brightness ratios of the system.

An observation with the ASCA satellite revealed a strong X-ray source, designated AXJ2019+112, towards MG2016+112 with an emission line at 3.5 keV which could correspond to FeXXV at $z = 0.92$ or FeXXVI at $z = 1.00$, the redshift of the lensing galaxy (Hattori et al. 1997, hereafter H97). The X-ray spectra results in an 8.6 keV gas temperature for a $z = 1.0$ source, implying a massive cluster ($M \approx 2 \times 10^{14}h^{-1}M_\odot$ at $r = 250h^{-1}$ kpc) at the redshift of the lens. Infrared and optical observations of the field (Lawrence et al. 1993, Langston et al. 1991, Schneider et al. 1985) revealed no excess of galaxies around the giant elliptical lens, the supposed brightest cluster galaxy (BCG), as would normally be found in a cluster. This led to the suggestion of a "dark cluster" associated with the lens, in which a cluster-sized dark matter and hot gas overdensity exists with few optically bright galaxies ($M/L_V > 2000M_\odot/L_\odot$). These observations were even more puzzling as the observed iron line in the X-ray spectra indicates a near-solar metallicity for the cluster, which implies a long history of star formation in the region (H97). A handful of galaxies at $z = 1.01$ have been found spectroscopically within a few arcminutes of the lens (Soucail et al. 2000), but these are not concentrated strongly around the lens.

Recently, B99 have found a slight overdensity of red galaxies using deep V, I, and K_s imaging in a region 200 kpc ($\sim 47''$) in radius around the QSO lens. Assuming that the galaxies they identified were the most luminous galaxies in a Schechter cluster luminosity function, they calculated that the total cluster luminosity was roughly ten times that of the BCG. Thus the proposed cluster has a mass-to-light ratio of only a few hundred solar, typical of what is seen in other massive high-redshift clusters (Luppino & Kaiser 1997, Clowe et al. 1998). The observed galaxies are red in both $V-I$ and $I-K_s$, suggesting a old stellar population and consistent with what is observed in other high-redshift clusters (Trentham & Mobasher 1998, van Dokkum et

Send offprint requests to: D. Clowe

⋆ Visiting Astronomer at the W. M. Keck Observatory, jointly operated by the California Institute of Technology and the University of California al. 1999). These observations, however, are based on only nine galaxies selected by two colors and confirmed by a third.

In this paper we present deep optical and infrared images in V, R, I, and K of the MG2016+112 field with the goals of testing the B99 selected galaxies with additional colors, detecting any additional, fainter cluster galaxies, and measuring the weak lensing signal in the field to confirm the presence and measure the mass of any cluster. In §2 we discuss the images taken and the image reduction process. We discuss the colors and magnitudes we measure for the proposed cluster galaxies of B99 as well as others in the field in §3. Section 4 contains a weak lensing analysis of the field. We summarize and discuss our major conclusions in §5.

Throughout this paper, unless stated otherwise, we assume $\Omega_0 = 1$, $\Lambda = 0$, and H_0 =100 km/s/Mpc.

2. Observations and Data Reduction

Deep I, R, and V-band imaging was performed on a field centered on MG2016+112 using LRIS (Oke et al. 1995) in direct imaging mode at the Keck II telescope on the nights of 1998 July 22-23. The resulting images cover a $6' \times 7.'5$ area in I and V and $7.'5 \times 7.'5$ area in R with $0.''215$ pixels. The total integration times are 1500s in I and V and 5400s in R, with seeing of $0.''50$, $0.''56$, and $0.''54$ FWHM in I, R, and V respectively.

The individual images in each filter were de-biased using the overscan strip and flattened with dome flats. The I-band images were then re-flattened with a medianed night-sky flat from a (relatively) empty piece of sky taken during the same nights to remove fringing. The images were then remapped with a bicubic polynomial to correct for focal plane curvature. The polynomial for the mapping was determined by requiring that the positions of the stars in each remapped frame were consistent to within 0.1 pixels ($\approx 0.''02$, the estimated rms error in the centroiding algorithm) rms with each other and within the errors of the positions of the stars in a Digital Sky Survey image and a catalog of stellar positions from the United States Naval Observatory. The mappings were then checked using a second group of stars which were not used to generate the polynomial. The re-mapping was performed using linear interpolation and a triangle method to distribute the original pixel values onto the new map. The method preserved surface brightness and has been tested to ensure that in the case of a fractional pixel shift with no change in the shape or size of the pixel that the second moments of the objects in the image are not shifted in a systematic manner (although there is some noise added).

The re-mapped images then had their sky subtracted by fitting a low order polynomial to the minima in the image. A final image was produced by averaging the sky-subtracted images with a sigma-clipping algorithm to remove cosmic rays. Photometry was determined by comparing the magnitudes of the bright but unsaturated stars with those in images of the field from the UH88″ telescope and Isaac Newton telescope which were calibrated from Landolt standards (Landolt 1992). We assume a Galactic extinction $A(B) = 0.81 \pm 0.12$ (Schlegel et al. 1998) and derive $A(V) \approx 0.61$, $A(R) \approx 0.46$, $A(I) \approx 0.29$,

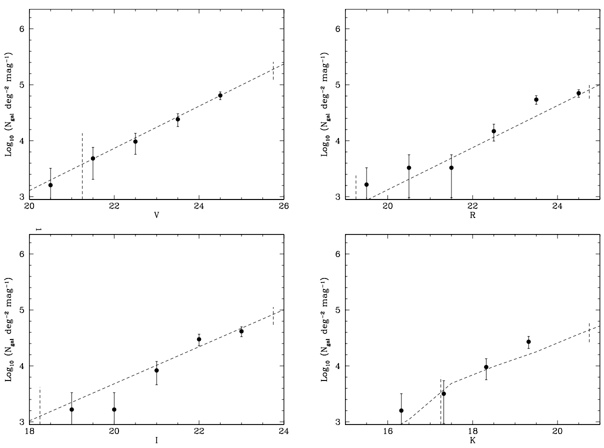

Fig. 1. Galaxy counts as a function of magnitude in the four observed passbands. All magnitudes are aperture magnitudes measured in an aperture of diameter 3.0 arcseconds, which are close to total magnitudes except for very bright galaxies, where we apply a small aperture correction to the measured magnitudes so that they approximate total magnitudes (which only happened for one foreground galaxy). The filled circles are the counts within $r = 225$ kpc radius from the QSO lens. The dashed lines represent typical mean background counts (Mobasher & Trentham 1998, Wilson et al. 1997). Approximate uncertainties in these lines are shown by the vertical dashed lines at two representative magnitudes (Mobasher & Trentham 1998, Trentham 1997).

and $A(K) \approx 0.07$, using the color conversions of Cardelli et al. (1989). The 5σ limiting magnitudes within a square $1.''0$ aperture are I=25.1, R=27.1, and V=27.1.

We also obtained deep K-band images using IRCAM3 at UKIRT on 1998 July 19-20. Each image is $1.'5$ on a side with $0.''286$ pixels. A 2×2 mosaic of pointings resulted in a $3'\times3'$ field with 9720s exposure time in each quadrant and an additional 3240s exposure time in the central $1.'5\times1.'5$. Individual exposures were 120s long and dithered by $8.''0$. The median seeing was about $0.''8$. Flat-field images were constructed using median-filtered dithered object frames from the whole night and sky images were constructed using sets of twenty-six 120s exposures. The individual frames were then flat-fielded, sky-subtracted and combined using a clipping algorithm that rejected bad pixels. Instrumental magnitudes were computed from observations of UKIRT faint standards (Casali & Hawarden 1992), giving a photometric accuracy in the zero-point of better than 2%. The 5σ limiting magnitude within a $1.''0$ square aperture in the reduced image is K=21.3.

3. Galaxy Counts and Color-Selection

The IMCAT (*http://www.ifa.hawaii.edu/~kaiser/imcat*) *hfindpeaks* detection algorithm was used to search for objects in the above $VRIK$ images. The objects were each inspected by eye in all images and spurious detections (due to stellar diffraction peaks, for example) were eliminated from the catalog of objects. Objects were identified as stars or galaxies on the basis of this inspection as well as using the measured half-light radii

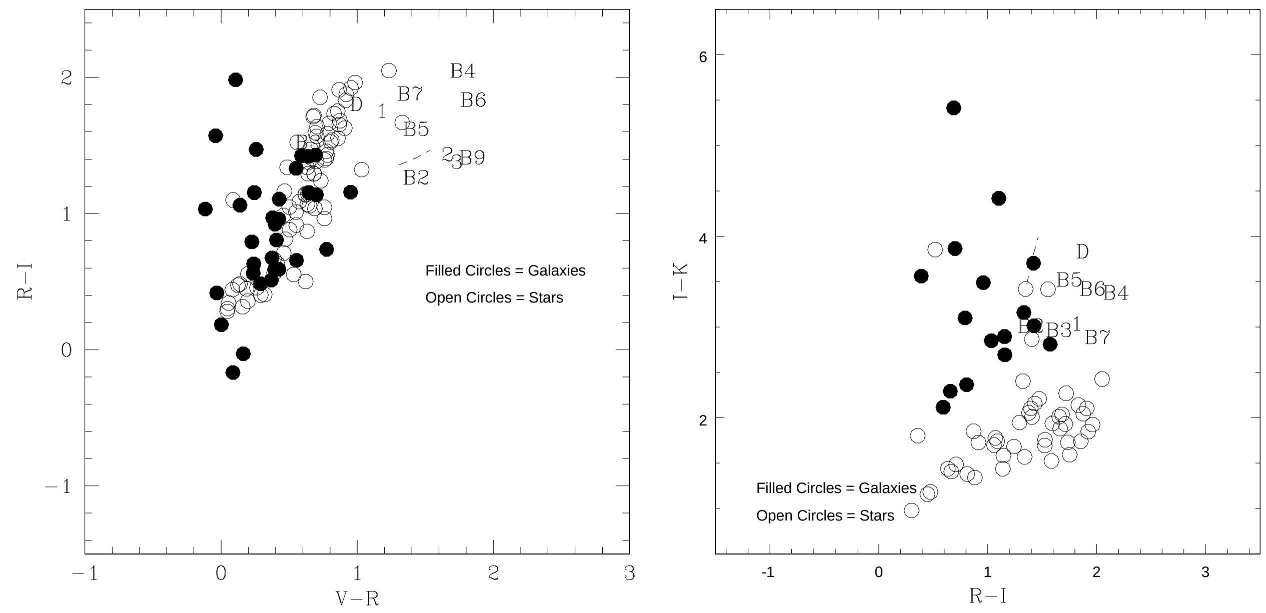

Fig. 2. Color-color diagrams for all objects with $K < 20$ for the RIK plot and $R < 24$ for the VRI plot which are less than 225 kpc from the QSO lens. Symbol D represents the positions for the four components of the lens galaxy. The symbols B# represent the positions of the red galaxies in Table 1 of B99 where # is the line number of the object in the table. The first object in their list is the same as object D. The eighth and ninth objects were not detected in our K-band image and the eighth object is believed to be a star from inspection of the optical bands. The symbols 1 through 3 represent new candidate red galaxies (2 and 3 were not detected in our K-band image either). The dashed line is where one expects passively evolving elliptical galaxies at $z = 1$ to reside, given the stellar population models of Kodama et al. (1998).

and central surface brightnesses compared to the total (large-aperture) magnitudes of the objects. Those objects which were classified as galaxies had their magnitudes remeasured using the IRAF *apphot* package, following a local sky subtraction. Uncertainties in these numbers are substantial at the faint end and come from uncertainties in the local sky due to scattered starlight, faint galaxy clustering, and Poisson noise. For example, objects at $R > 24$ typically have uncertainties of at least 0.5 magnitudes in each color, measured by using apertures of various sizes and radii around the objects to determine the local sky value.

Fig. 1 shows the galaxy number counts as a function of magnitude for this field in each filter. There is no obvious excess of galaxies above the background, as was seen in the rich cluster MS1054−03 at $z = 0.83$ (Trentham & Mobasher 1998), but the background uncertainty on these small scales is large. Thus, the background counts might be anomalously low, and a cluster at $z = 1$ may still exist despite the lack of an excess. The most straightforward way to look for such a cluster is to (i) look for dense groups of galaxies very close to the lensing galaxy D, and (ii) inspect color-color and color-magnitude diagrams. These are presented in Fig. 2 and Fig. 3.

We identified one group of seven faint objects all between 19 and 27 kpc from galaxy D in the R-band image. The brightest of these is $R \approx 24$ and the rest around $R \approx 26$ and all, except the brightest, were too faint to be detected in the other filters. The brightest has $R - I$ and $I - K$ colors of 1.57 and 2.81, which are somewhat bluer than those of galaxy D (1.81 and 3.83). From the colors it is unlikely that these would be the brightest galaxies in a higher redshift cluster. From the observed number density of $24 < R < 26$ galaxies in this field, the chances of projecting seven unrelated galaxies in such a small area is only 0.14%. However, with the exception of the brightest object, which is spatially extended and therefore, probably, a galaxy, we cannot determine if the objects are stars or galaxies. Two other objects also around $R \approx 26$ are located on the eastern side of galaxy D at roughly the same distance. Even assuming that these objects are galaxies and associated with galaxy D, the proposed 8 keV cluster with galaxy D as the brightest cluster galaxy would still have a low surface density of cluster galaxies near the BCG as compared to high-redshift clusters of similar mass (both MS1137+66 and RXJ1716+67, ∼6 keV clusters at $z \sim 0.8$, have roughly twice as many galaxies within 30 kpc of the BCG). We note, however, that as MG2016+112 was originally discovered as a medium-separation QSO lens, that this deficiency of bright cluster galaxies near the BCG may be a selection effect as a large number of massive galaxies would perturb the lensing caustics sufficiently to preclude a double image of the QSO from lensing by the BCG.

From Fig. 2 and Fig. 3, one can find a number of red galaxies having approximately the correct $I - K$ to be old stellar populations at $z = 1$ (Kodama et al. 1998) within $225h^{-1}$ kpc of galaxy D. Of these, eight are the red objects described by B99, including galaxy D, and three are not found in the B99 sample. One of the B99 objects, the eighth in their Table 1, we identified as a star. Our revised count of the total number of candidate members from color selection is thus eleven. There are only fifteen galaxies in the image outside the selected region with col-

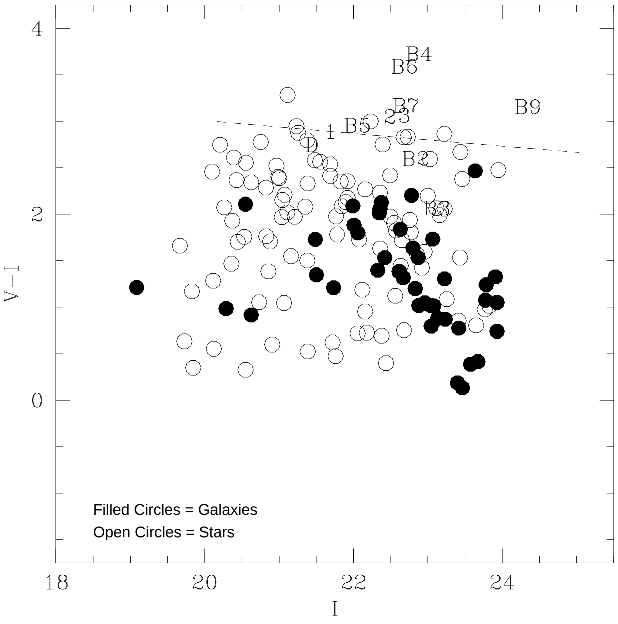

Fig. 3. The $V-I$ vs. I color-magnitude diagram of all objects less than 225 kpc from the QSO lens. The symbols have the same meaning as in Fig. 2. The dashed line is where one would expect passively evolving elliptical galaxies at $z=1$ to reside, given the stellar population models of Kodama et al. (1998).

ors and magnitudes similar to the selected galaxies. This gives an overdensity around galaxy D of $1160^{+440}_{-260}\%$ compared to the rest of the image, and the probability this is due to Poissonian fluctuations in the density is 3×10^{-12}. If cluster members, as argued by B99, these are presumably responsible for generating the metals seen at X-ray wavelengths by H97. Spectroscopic redshifts would be needed to confirm this interpretation.

We note, however, that these galaxies are up to a magnitude redder in $R-I$ than would be predicted for passively-evolving ellipticals. This is probably due in part to photometric uncertainties, but could also be due to small amounts of internal extinction. Note that at $z=1$ the $R-I$ color of a pure old stellar population is anomalously red since at this redshift the 4000Å break falls exactly between these two passbands, which in turn means that this color is particularly susceptible to being made significantly different by internal extinction. In addition, galaxies bluer than the ones discussed by B99 could in principle also be members that are undergoing current star formation. Again, spectroscopic information will be useful to investigate these possibilities further.

4. Weak Lensing Analysis

4.1. Techniques

The first step in the weak lensing analysis of the field is to detect and measure the shapes of the background galaxies. This was done using the R-band image, which is of similar depth and resolution to other Keck fields which have successfully reconstructed the surface mass density of other high-redshift clusters (Clowe et al. 1998, 2000). Most of this analysis was done using the IMCAT software package.

Prior to using a detection algorithm on the image, we first subtracted small-scale background fluctuations in the image, caused primarily by stellar halos and scattered star light. These fluctuations were determined by smoothing an image of the local minima of the sky values with a $5''$ Gaussian, and dividing by an image smoothed on the same scale which contained the mask of the pixels detected as minima. In addition to removing any sky variations, this routine typically removed extended wings of bright stars in the image as well as any large, low surface brightness objects which might have been present. Performing this step was necessary as the detection algorithm can get confused by rapid changes in the sky background.

To detect the faint galaxies we used a hierarchical peak-finding algorithm which provided a position, luminosity, and size estimate for each object (Kaiser et al. 1995, hereafter KSB). Local sky levels around each object were calculated after excluding all pixels within three detection radii of an object in the catalog. The luminosity was measured using a circular aperture equal to three times the smoothing radius at which the object achieved maximum significance. I and V magnitudes were measured using the same sky-subtraction technique and the same aperture radius. Noise peaks and merged objects were removed from the catalog by requiring a minimum signal-to-noise at maximum detection significance of 10, rejecting abnormally large and small objects, rejecting objects with extremely high ellipticities, and by visual inspection. The ellipticities of each object were measured using optical polarizations $e_\alpha = \{I_{11}-I_{22}, 2I_{12}\}/(I_{11}+I_{22})$ formed from the quadrupole moments $I_{ij} = \int d^2\Theta W(\Theta)\Theta_i\Theta_j f(\Theta)$ where f is the flux density and $W(\Theta)$ is a Gaussian weighting function of a scale equal to the smoothing radius at which the object was detected with maximum significance (KSB).

The next step in the lensing analysis was to remove the PSF anisotropies and smearing. Due to the large number of stars in the field (the final sample was 675 bright, unsaturated stars with no neighbors within $10''$), we were able to fit the stellar ellipticities across the field with an arbitrarily high-order two-dimensional polynomial. We used third, fifth, and seventh order polynomials for the fits, and subtracted the fit values from all detected objects via the method in KSB. We then applied the boost factor discussed below to the stellar ellipticities, and used the boosted ellipticities to measure any false signal which will be induced in the data by the residual PSF anisotropies. As can be seen in Fig. 5, there is a small positive signal in the center of the fields; however the magnitude of this signal is small compared to the noise caused by the intrinsic ellipticity distribution of the background galaxies, and thus should not significantly affect any observed lensing signal. The amplitude of the false residual signal decreases somewhat with the increasing order of the polynomial fit to the ellipticities, as can be seen in Fig. 5, and thus we used the bi-septic polynomial fit to correct the ellipticities of the galaxies. This correction was done by subtracting the value of the fit at the position of each galaxy from the measured

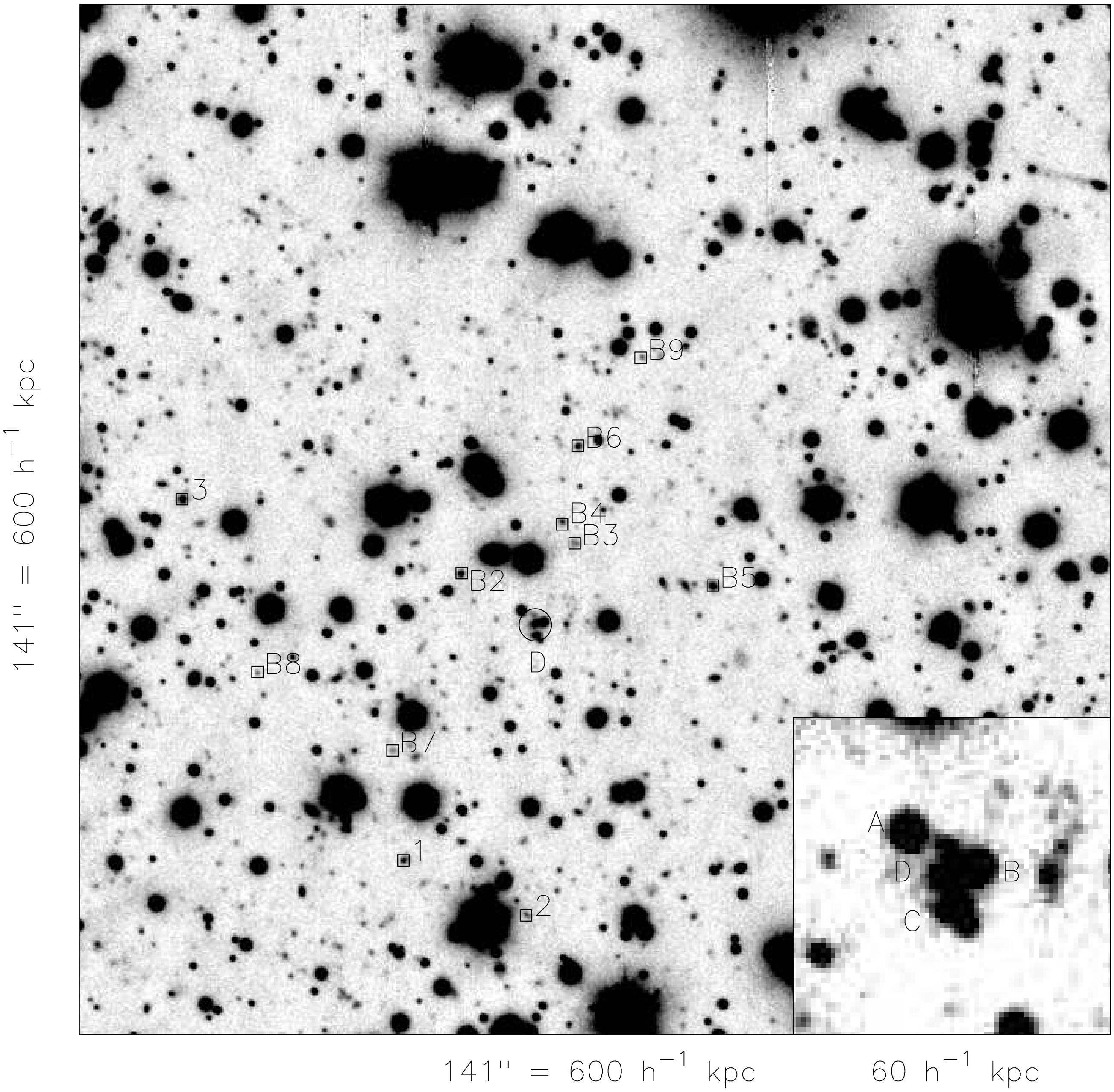

Fig. 4. The central $600h^{-1}$ kpc ($141''$) of the R-band image is shown above, plotted using a $\sqrt{\log}$ stretch, with north being up and east to the left. Objects identified as galaxies with colors consistent with the QSO lensing galaxy have boxes drawn around them. Inset in the south-west corner is a close-up of the QSO lens, showing the cluster of faint objects north-west of the lens system.

ellipticity, after scaling the fit value by $P_{sm}/P^{\star}_{sm}$. As defined in KSB (corrections in Hoekstra et al. 1998), P_{sm} is a quasi-tensor which describes how the ellipticity of an object changes under an applied anisotropy and the asterisk denotes the typical value for a star in the image.

To correct for the reduction of the ellipticities from circular smearing by the PSF, we calculated a boost factor for each galaxy $P_\gamma = P_{sh} - P_{sm}(P^{\star}_{sh}/P^{\star}_{sm})$ (Luppino & Kaiser 1997), where P_{sh} is a quasi-tensor describing how the ellipticity of an object changes with an applied shear (KSB), and P_{sm} and the asterisk are defined as above. Due to the large anisotropy in the stars at the edges of the Keck field, we computed $P^{\star}_{sh}$ and $P^{\star}_{sm}$ only in the central region with a diameter of one thousand pixels, in which there was no significant anisotropy. As the individual values of P_γ are quite noisy for faint galaxies, we fit P_γ with a third order polynomial as a function of size and ellipticity. Because of noise and a tendency of the sky-subtraction algorithm to measure slightly too large a sky value (owing to the presence of many faint, unresolved objects), very faint galaxies tend to have artificially low, sometimes even negative, P_γ values. We corrected for this by applying a cut to the fitted P_γ values such that any object with a detected size smaller than that

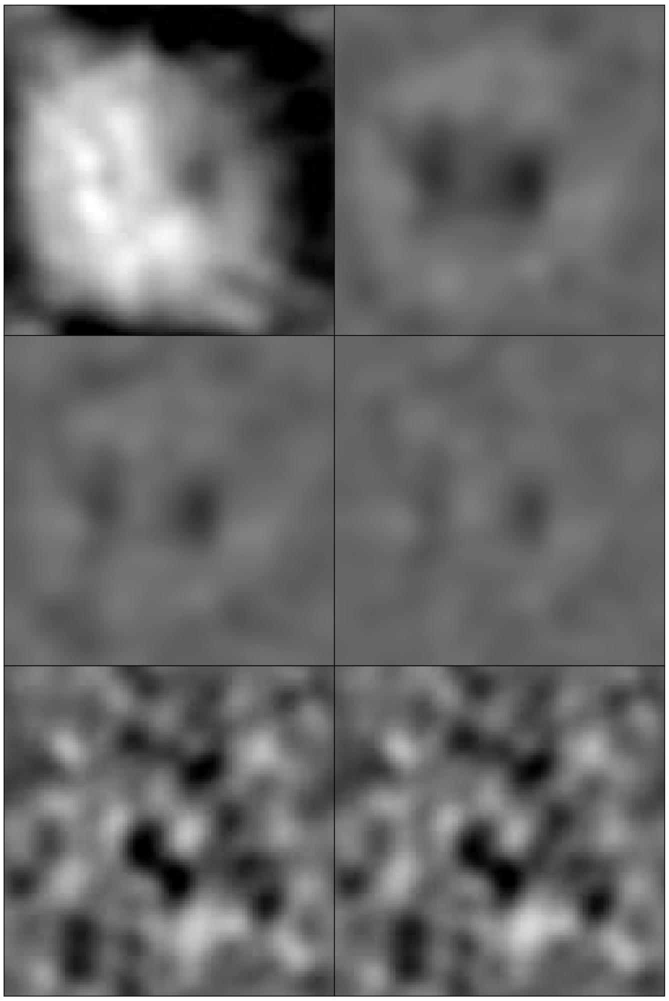

Fig. 5. κ measured from stars in the field. The top-left panel is the signal from the uncorrected ellipticities. In the top-right panel the ellipticities have had a bi-cubic fit subtracted. The middle panels have the ellipticities corrected with a bi-pentic and bi-septic fit for the left and right panels respectively. The bottom panels are mass reconstructions using the background galaxies from the mass reconstruction in Fig. 7, but applying a random orientation to each galaxy while preserving the modulus of the ellipticity, and thus is a good indication of the noise level seen in the reconstructions from the intrinsic ellipticity distributions of the background galaxies. The left-hand image is the original reconstruction and the right-hand image has the reconstruction for the seventh-order corrected stellar ellipticities added to it. The greyscale is the same for all the panels, with black meaning positive (false) mass.

of the stars in the field was assigned a P_γ equal to that of galaxies with detected sizes similar to that of stars, 0.2 in this case. We choose to apply this correction instead of removing the objects from the catalog as the faintest galaxies should be at the highest mean redshift, and therefore show the greatest amount of gravitational shearing. This artificial cutoff in P_γ is equivalent to applying a weight function in all subsequent operations such that the galaxies with measured sizes smaller than stellar are given a lower weight.

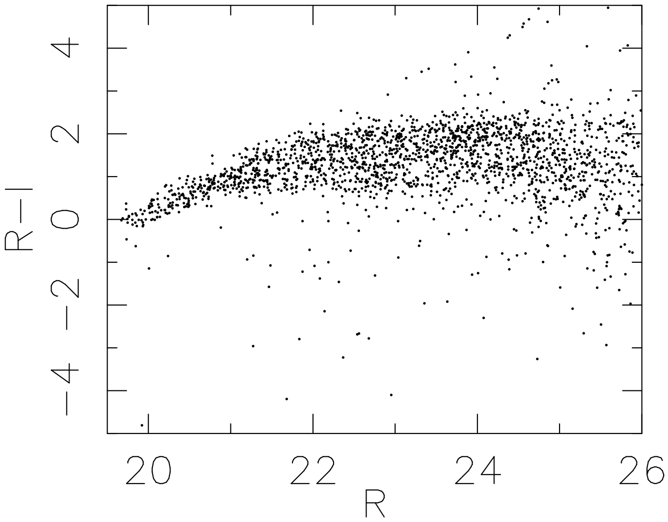

Fig. 6. $R - I$ vs. R color-magnitude diagram of all objects detected with a half-light radius the same as the bright stars. For $R < 24$, this will be almost entirely stars while for $R > 24$ small galaxies will be included in the objects.

We then created an estimate of the shear for each galaxy $\hat{\gamma}_\alpha = e_\alpha / P_\gamma$. Both the shear γ and convergence κ are second derivatives of the surface potential, $\gamma_\alpha = {}^1\!/_2\{\phi_{,11} - \phi_{,22}, 2\phi_{,12}\}$ and $\kappa = \Sigma/\Sigma_{crit} = {}^1\!/_2\nabla^2\phi$ where $\Sigma_{crit}^{-1} = 4\pi G c^{-2} D_l D_{ls} D_s^{-1}$. Thus, one can create a two dimensional map of the convergence by Fourier transforming shear estimates, multiplying by the appropriate conversion factors, and retransforming (Kaiser & Squires 1993). The surface density can then be extracted from the convergence, providing one knows both the redshift of the lens and the redshift distribution of the background galaxies. The intrinsic ellipticities of the galaxies cannot be removed from the shear estimate, and are the dominant source of noise in the analysis.

4.2. Results

Previous work on lensing by $z \sim 0.8$ clusters has shown that to maximize the signal-to-noise of the lensing one must use faint blue galaxies (Luppino & Kaiser 1997; Clowe et al. 1998, 2000) as these are presumably at higher redshifts than the brighter and redder galaxies, and thus have been subjected to a stronger shear. Also, because of the large number of stars in this field, one must also apply a selection in color to exclude the majority of the stellar population, which still has a significant contribution at the faintest observable magnitudes (as seen in Fig. 6). As a result we selected as our background sample all galaxies with $24.20 < R < 26.70$ and $R - I < 0.35$ ($23.64 < R < 26.14$ and $R - I < 0.55$ after correcting for Galactic extinction). This resulted in a catalog of 910 galaxies ($\sim$ 17 per sq. arcminute), which is less than half the counts expected from the color and magnitude cuts because of incompleteness at the faint end and loss of area due to extended stellar halos. The rms ellipticity of this galaxy sample, after the corrections for psf effects

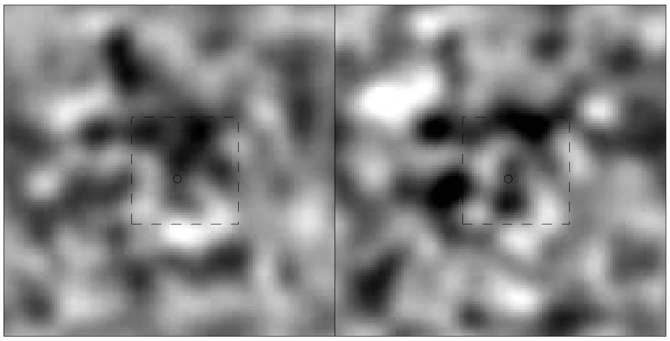

Fig. 7. The weak lensing κ reconstructions, using the KS93 algorithm, is shown above. Positive κ peaks are black, and the dashed square indicates the area of the reconstruction corresponding to the image shown in Fig. 4. The circle indicates the position of the QSO lens. The left-hand map uses objects detected in the R-band image, and the right-hand map uses objects detected in the combined $R + V$ image.

described above, is ~ 0.4, which combined with the number counts gives an rms shear in a square arcminute area of ~ 0.1.

The weak lensing mass reconstruction from the background galaxy catalog is shown in Fig. 7. This was created using the KS93 algorithm (Kaiser & Squires 1993), which uses the Fourier transform method described earlier to convert shear to convergence. This algorithm can only determine κ to an unknown additive constant and suffers from biasing at the edges of the frame, but the intrinsic ellipticity distribution of the galaxies is translated into white noise across the field.

As can be seen in Fig. 7, we do detect an overdensity of mass in the field, although its center is $60''$north and $24''$east of the position of the QSO lens. The rest of the peaks seen in the reconstruction are at the level of the expected noise due to the low number density of background galaxies. One way to check that the peak is real and not caused by a small number of high ellipticity galaxies is to randomly divide the background galaxy catalog in two and see if the peak is present in both of the sub-catalogs. We did this ten times, and in all twenty sub-catalogs we detect the mass peak albeit with changes in the shape, position, and amplitude as expected by the increased noise in the reconstruction due to the lower background galaxy number density. The other peaks in the field tended to vary in amplitude and often disappear in the sub-catalog reconstructions, which suggests that they are caused primarily by a handful of galaxies and not a real lensing signal.

We also performed a lensing analysis using an image made from both the R and V images added together. This allowed us to detect $\sim 20\%$ more galaxies using the same signal-to-noise, R magnitude, and $R - I$ color cuts as given above. The lensing reconstruction for this is also shown in Fig. 7. The extra galaxies and change in the noise properties of the original galaxies results in only a small change in the amplitude of the main peak but a much larger change in the smaller, presumably noise, peaks. We also attempted the same using R and I, and V, R, and I images added together, but the higher sky noise in the I frames resulted in a severe decrease in the number of faint galaxies detected. For the rest of the results we will quote the

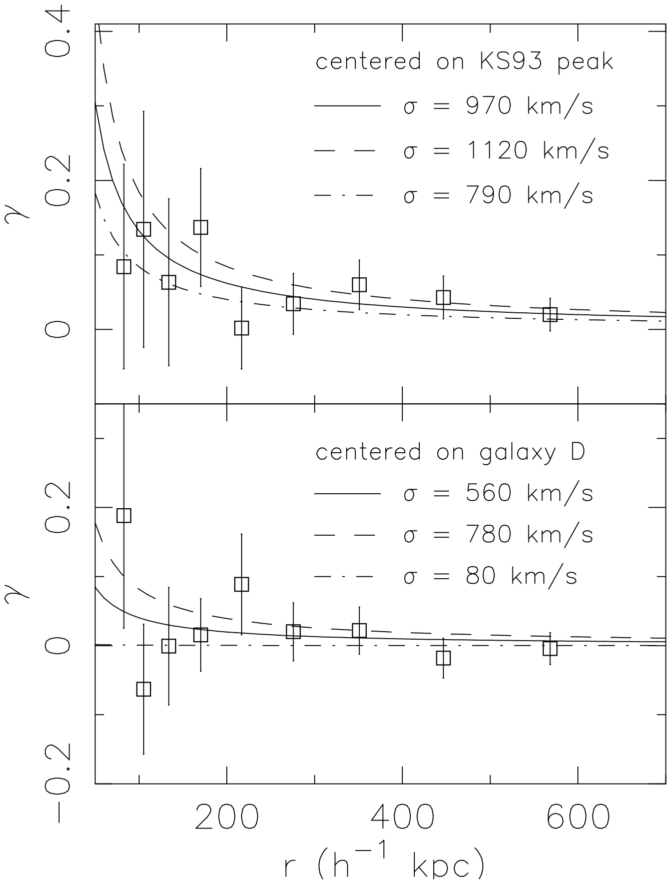

Fig. 8. The radial shear profiles centered on the peak of the KS93 κ reconstruction (top) and the QSO lens (bottom). The solid lines show the best fit singular isothermal sphere profile assuming $z_{bg} = 1.5$ and $z_{lens} = 1$ and the dashed lines are the 1σ limits determined by $\delta\chi^2$ of the fits.

numbers taken from just the R image, but all of the results from the $R + V$ image agree within errors to those of the R image.

To better quantify the strength and significance of the observed overdensity, as well as to detect any low-significance signal at the position of the QSO lens, we computed the azimuthally-averaged tangential shear of the background galaxies as a function of radius from a given position. We can then fit these radial shear profiles with various models and measure the $\delta\chi^2$ between the best fit model and a zero shear model to determine the significance of the peaks. The radial shear profiles centered on the peak seen in the mass reconstruction and on the QSO lens are given in Fig. 8, as well as the best fit isothermal sphere models. For these models we assumed a lens redshift of 1 and background galaxy redshift of 1.5. The z_{bg} = 1.5 assumption was derived by calculating

$$\bar{\Sigma}_{crit}(z_b g) = \frac{\int n(z) dz}{\int \frac{n(z)}{\Sigma_{crit}(z)} dz} \tag{1}$$

where $n(z)$ is from the HDF south photometric redshift survey of Fontana et al. (1999) using the same magnitude and color cuts as used in the data, after correction for Galactic extinction.

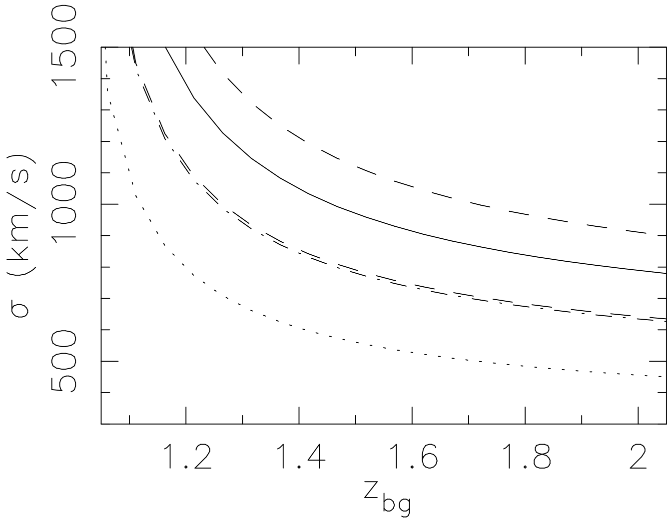

Fig. 9. The best fit singular isothermal sphere velocity dispersion to the observed shear when centered on the KS93 mass peak (solid line) and QSO lens (dotted line) as a function of mean background galaxy redshift, assuming the lens is at $z = 1.01$. The dashed and dash-dotted lines give the 1σ limits for the two centers, respectively.

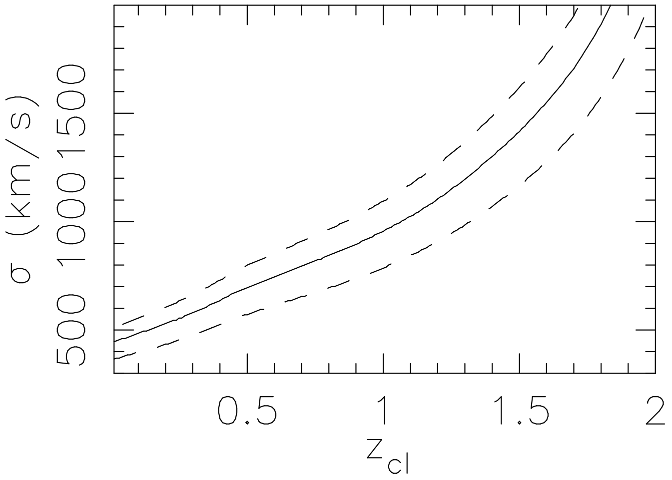

Fig. 10. The best fit singular isothermal sphere velocity dispersion to the observed shear centered on the KS93 mass reconstruction peak as a function of lens redshift. The background galaxies are assumed to have the same redshift distribution as those of similar magnitude and redshift in the Fontana et al. (1999) HDF-S photometric redshift catalog. The dashed lines give the 1σ limits to the fits.

Altering these assumptions will change the velocity dispersion, and thus the mass, of the lens model, but does not significantly change the χ^2 or the significance of the peak.

The best fit isothermal sphere model for the observed peak, centered on the peak in the KS93 reconstruction, has $v = 970$ km/s, $\chi^2/(n-1) = 1.02$, and $\delta\chi^2$(0 km/s $-$ 970 km/s) = 8.95, and thus is at nearly 3σ significance. The highest significance in the field using this statistic occurs 5.″6 east and 14.″2 north of the KS93 peak (18.″3 west and 71.″6 north of the QSO lens), with $\sigma = 1040$ km/s, $\chi^2/(n-1) = 0.62$, and $\delta\chi^2$(0 km/s - 1040 km/s) = 9.23. The difference between the maxima in the two techniques is a result of the KS93 reconstruction using all of the galaxies in the frame while the tangential shear uses only those between 17.″2 and 150.″5 from the central position, and that the contributions from the galaxies are weighted in different manners. The best fit isothermal sphere model when the shear profile is centered on the QSO lens has $\sigma = 560$ km/s, $\chi^2/(n-1) = 1.13$, and $\delta\chi^2$(0 km/s $-$ 560 km/s) = 1.05, and therefore has only 1σ significance. The best fit velocity dispersion, as well as the one-σ deviations, as a function of background galaxy redshift is given in Fig. 9.

To test the significances of the peaks given by the $\delta\chi^2$ of the isothermal sphere fits we performed Monte Carlo simulations in which we kept the positions and moduli of the ellipticities of the background galaxies fixed, but applied a random spin to their orientations. We then measured the best isothermal sphere fits to the tangential shear profiles using the central position from the KS93 reconstruction. The resulting best fit isothermal sphere models were a Gaussian distribution around $v^2 = 0$ km^2/s^2. Only 128 of the 100,000 realizations resulted in a best fit model with $\sigma \geq 970$ km/s, which corresponds to a significance level of 3σ, in agreement with the $\delta\chi^2$ significance level.

To determine the significance of not detecting a peak at the position of the QSO lens we performed a similar process to the above. We again kept the positions and moduli of the ellipticities of the background galaxies fixed and randomized their orientations, but then we also applied a shear to the background galaxies. The applied shear was calculated for each galaxy's position by using a 1000 km/s isothermal sphere centered on the QSO lens with $z_{lens} = 1$ and $z_{bg} = 1.5$. Only 5031 of the 100,000 realizations resulted in a best fit model with $\sigma \leq 560$ km/s, which corresponds to 2.0σ significance.

5. Conclusions

We have detected in $VRIK$ images ten galaxies with colors consistent with the lensing galaxy of the MG2016+112 QSO lens within $225h^{-1}$ kpc of the lensing galaxy. This represents an increase in number density of $1160^{+440}_{-260}\%$ (1σ error on the background density) compared to galaxies of similar colors and magnitudes in the rest of the image. We also find nine faint objects, seven of them grouped in a small area, within $30h^{-1}$ kpc of the lens galaxy D. Due to their faintness, we are unable to measure colors or determine if they are galaxies or stars except for the brightest of the nine which is a galaxy and somewhat bluer than galaxy D. Even assuming all of these galaxies are associated with the lens galaxy D, they would total a small fraction of the galaxy counts associated with the clusters MS1137+66 and RXJ1716+67, both at $z \sim 0.8$ and of similar X-ray properties as those measured for AXJ2019+112 (Donahue et al. 2000; Henry et al. 1998; H97), using the same radial, magnitude, and color cuts adjusted to the cluster BCGs and redshifts.

We have also made a mass reconstruction of the field from faint blue galaxies. We find a peak of comparable mass to that given by the X-ray observations, but the center of the peak is over an arcminute north-west of the lens galaxy D ($272h^{-1}$ kpc at $z = 1$). This peak has a best fit singular isothermal sphere model of $\sigma = 970$ km/s and is significant at 3σ. We can rule out a 1000 km/s singular isothermal sphere, the mass expected from the X-ray observations, centered on the lens galaxy D at 2.0σ significance. We do not see any evidence for a group of similarly colored galaxies in the vicinity of the observed mass peak, but this region is highly obscured by bright stars. We plot in Fig. 10 the velocity dispersion of a singular isothermal sphere needed to provide the observed lensing signal as a function of redshift of the lens.

Finally, we note that the 1σ upper mass limit centered on galaxy D from weak lensing is near the 1σ lower mass limit from the X-ray data. Thus the best measure of the mass of the cluster from the two data sets would give a velocity dispersion of $\sigma \sim 800$ km/s.

Acknowledgements. We wish to thank Genevieve Soucail, Jean-Paul Kneib, Narciso Benitez, Tom Broadhurst, and Piero Rosati for providing information and data on this field prior to publication. We also wish to thank Tadayuki Kodama and Peter Schneider for their advice and help. Some of the data presented herein were obtained at the W.M. Keck Observatory, which is operated as a scientific partnership among the California Institute of Technology, the University of California and the National Aeronautics and Space Administration. The Observatory was made possible by the generous financial support of the W.M. Keck Foundation. The United Kingdom Infrared Telescope is operated by the Joint Astronomy Centre on behalf of the U.K. Partical Physics and Astronomy Research Council. We acknowledge assistance from the Isaac Newton Group Service Programme in providing photometric zero points for the optical data, from the Isaac Newton Telescope on La Palma. DC acknowledges the "Sonderforschungsbereich 375-95 für Astro–Teilchenphysik" der Deutschen Forschungsgemeinschaft for finacial support. NT acknowldedges the PPARC for financial support. This work was supported by the TMR Network "Gravitational Lensing: New Constraints on Cosmology and the Distribution of Dark Matter" of the EC under contract No. ERBFMRX-CT97-0172.

References

Benitez, N., Broadhurst, T., Rosati, P., et al., 2000, ApJ, in press
Cardelli, J., Clayton, G., Mathis, J., 1989, ApJ, 345, 245
Casali, M.M., Hawarden, T.J., 1992, JCMT-UKIRT newsletter, 3, 33
Clowe, D., Luppino, G., Kaiser, N., et al., 1998, ApJ, 497, L61
Clowe, D., Luppino, G., Kaiser, N., et al., 2000, ApJ, in press
Donahue, M., Voit, G.M., Scharf, C.A., et al., 2000, ApJ, in press
Fontana, A., D'Odorico, S., Fosbury, R., et al., 1999, A& A, 343, 19
Garrett, M.A., Porcas, R.W., Nair, S., et al., 1996, MNRAS, 279, L7
Hattori M., Ikebe Y., Asaoka I., et al., 1997, Nat, 388, 146
Henry, J.P., Gioia, I.M., Mullis, C.R., et al., 1998, AJ, 114, 1293
Hoekstra, H., Franx, M., Kuijken, K., et al., 1998, ApJ, 504, 636
Kaiser, N., Squires, G., 1993, ApJ, 404, 441
Kaiser, N., Squires, G., Broadhurst, T., 1995, ApJ, 449, 460
Kodama T., Arimoto N., Barger A.J., et al., 1998, A& A, 334, 99
Landolt, A.U. 1992, AJ, 104, 340
Langston, G., Fischer, J., Aspin, C., 1991, AJ, 102, 1253
Lawrence, C.R., Neugebauer, G., Matthews, K., 1993, AJ, 105, 17
Lawrence, C.R., Schneider, D.P., Schmidt, M., et al., 1984, Sci, 223, 46
Luppino, G.A., Kaiser, N., 1997, ApJ, 475, 20
Mobasher, B., Trentham, N., 1998, MNRAS, 293 315
Nair, S., Garrett, M.A., 1997, MNRAS, 284, 58
Narasimha, D., Chitre, S.M., 1989, AJ, 97, 327
Oke, J.B., Cohen, J.G., Carr, M., et al., 1995, PASP, 107, 375
Schlegel D.J., Finkbeiner D.P., Davis M., 1998, ApJ, 500, 525
Schneider D.P., Lawrence C.R., Schmidt M., et al., 1985, ApJ, 294, 66
Schneider D.P., Gunn, J.E., Turner, E.L., et al., 1986, AJ, 91, 991
Soucail G., Kneib J.-P., Jansen A.O., et al., 2000, in prep
Trentham, N., 1997, MNRAS, 286, 133
Trentham, N., Mobasher, B., 1998, MNRAS, 299, 488
van Dokkum, P.G., Franx, M., Fabricant, D., et al., 1999, ApJ, 520, L95
Wilson, G., Smail, I., Ellis, R. S., et al., 1997, MNRAS, 284, 915